

Nonlinear magnetohydrodynamic effects on Alfvén eigenmode evolution and zonal flow generation

This article has been downloaded from IOPscience. Please scroll down to see the full text article.

2010 Nucl. Fusion 50 084016

(<http://iopscience.iop.org/0029-5515/50/8/084016>)

View [the table of contents for this issue](#), or go to the [journal homepage](#) for more

Download details:

IP Address: 128.83.61.126

The article was downloaded on 07/10/2010 at 22:01

Please note that [terms and conditions apply](#).

Nonlinear magnetohydrodynamic effects on Alfvén eigenmode evolution and zonal flow generation

Y. Todo^{1,2}, H.L. Berk³ and B.N. Breizman³

¹ National Institute for Fusion Science, Toki, Gifu 509-5292, Japan

² The Graduate University for Advanced Studies (SOKENDAI), Toki, Gifu 509-5292, Japan

³ Institute for Fusion Studies, University of Texas at Austin, Austin, TX 78712, USA

E-mail: todo@nifs.ac.jp

Received 13 November 2009, accepted for publication 16 February 2010

Published 28 July 2010

Online at stacks.iop.org/NF/50/084016

Abstract

Nonlinear magnetohydrodynamic (MHD) effects on Alfvén eigenmode evolution were investigated via hybrid simulations of an MHD fluid interacting with energetic particles. The investigation focused on the evolution of an $n = 4$ toroidal Alfvén eigenmode (TAE) which is destabilized by energetic particles in a tokamak. In addition to fully nonlinear code, a linear-MHD code was used for comparison. The only nonlinearity in that linear code is from the energetic-particle dynamics. No significant difference was found in the results of the two codes for low saturation levels, $\delta B/B \sim 10^{-3}$. In contrast, when the TAE saturation level predicted by the linear code is $\delta B/B \sim 10^{-2}$, the saturation amplitude in the fully nonlinear simulation was reduced by a factor of 2 due to the generation of zonal ($n = 0$) and higher- n ($n \geq 8$) modes. This reduction is attributed to the increased dissipation arising from the nonlinearly generated modes. The fully nonlinear simulations also show that geodesic acoustic mode is excited by the MHD nonlinearity after the TAE mode saturation.

PACS numbers: 52.35.Bj, 52.35.Mw, 52.55.Pi, 52.65.Ww

(Some figures in this article are in colour only in the electronic version)

1. Introduction

The destabilization of Alfvén eigenmodes by energetic particles is an important concern for burning plasmas since the excited modes can enhance transport and losses of energetic ions. Computer simulation is a powerful tool to investigate the interaction between Alfvén eigenmodes and energetic particles. We performed the first numerical demonstration of toroidal Alfvén eigenmode (TAE) bursts [1] with parameters similar to a TFTR experiment [2] and many of the experimental characteristics were reproduced. These include (a) the synchronization of multiple TAEs, (b) the modulation depth of the drop in the stored beam energy and (c) the stored beam energy. However, the saturation amplitude was $\delta B/B \sim 2 \times 10^{-2}$, which is higher than the value $\delta B/B \sim 10^{-3}$ inferred from the experimental plasma displacement measurements [1, 3]. In the simulation of [1], the only nonlinearity retained was the nonlinearity in the energetic-particle orbits, while the nonlinear magnetohydrodynamic (MHD) effects were neglected. Thus the spatial profiles and damping rates of the TAEs were assumed to be independent of the mode amplitude. Such a simulation is justified when particle trapping is the

most important saturation mechanism for the TAE instability [4, 5]. This saturation mechanism has been demonstrated in several previous simulations [6–9]. However, the linear simulation tends to give too large a saturation level. This suggests that the MHD nonlinearity neglected in the TAE burst simulation may be important and is well worth investigating carefully. In another simulation study of TAE bursts, where the MHD nonlinear effects are taken into account but the parameters are not very close to the experiment, the saturation level is roughly $\delta B/B \sim 5 \times 10^{-3}$ [10]. The effects of MHD nonlinearities on the increase in TAE damping rate were investigated theoretically [11] and numerically [12]. These studies further motivated us to investigate the nonlinear MHD effects on the TAE evolution to better understand the physics mechanism of saturation.

In this work we study the nonlinear evolution of a single linearly unstable TAE mode with toroidal mode number $n = 4$ using two versions of the MEGA code [13–15] which is a hybrid simulation code for an MHD fluid interacting with energetic particles. With the standard version of the MEGA code, the full nonlinear dynamics of both the MHD fluid and the energetic particles is simulated. In the other version of

the MEGA code, only linear-MHD equations are used while the nonlinear particle dynamics is retained. We shall refer to this version as the linear-MHD simulation. A comparison of the results between the nonlinear MHD and linear-MHD simulations is used to clarify how the MHD nonlinearities affect the TAE evolution. We demonstrate that the nonlinearly generated modes, both the zonal ($n = 0$) and the higher- n ($n \geq 8$) modes, reduce the TAE saturation level. To understand the underlying physics mechanism, we analysed the energy dissipation from each toroidal mode number. We found that the total energy dissipation is significantly increased by the nonlinearly generated modes. The increase in the total energy dissipation reduces the TAE saturation level. The spatial profiles and the evolution of the nonlinearly generated $n = 0$ and $n = 8$ modes are investigated. After the saturation of the TAE instability a geodesic acoustic mode (GAM) is observed, driven by the MHD nonlinearity.

2. The simulation model

Several hybrid simulation models have been constructed [7, 16–18] to study the evolution of Alfvén eigenmodes destabilized by energetic particles. In the MEGA code, the bulk plasma is described by the nonlinear MHD equations and the energetic ions are simulated with the δf particle method. The MHD equations with the energetic-ion effects are given by

$$\frac{\partial \rho}{\partial t} = -\nabla \cdot (\rho \mathbf{v}) + \nu_n \Delta (\rho - \rho_{eq}), \quad (1)$$

$$\begin{aligned} \rho \frac{\partial \mathbf{v}}{\partial t} = & -\rho \vec{\omega} \times \mathbf{v} - \rho \nabla \left(\frac{v^2}{2} \right) - \nabla p + (\mathbf{j} - \mathbf{j}'_h) \mathbf{B} \\ & + \frac{4}{3} \nabla (\nu \rho \nabla \cdot \mathbf{v}) - \nabla \times (\nu \rho \vec{\omega}), \end{aligned} \quad (2)$$

$$\frac{\partial \mathbf{B}}{\partial t} = -\nabla \times \mathbf{E}, \quad (3)$$

$$\begin{aligned} \frac{\partial p}{\partial t} = & -\nabla \cdot (p \mathbf{v}) - (\gamma - 1) p \nabla \cdot \mathbf{v} \\ & + (\gamma - 1) \left[\nu \rho \omega^2 + \frac{4}{3} \nu \rho (\nabla \cdot \mathbf{v})^2 + \eta \mathbf{j} \cdot (\mathbf{j} - \mathbf{j}_{eq}) \right] \\ & + \nu_n \Delta (p - p_{eq}), \end{aligned} \quad (4)$$

$$\mathbf{E} = -\mathbf{v} \times \mathbf{B} + \eta (\mathbf{j} - \mathbf{j}_{eq}), \quad (5)$$

$$\mathbf{j} = \frac{1}{\mu_0} \nabla \times \mathbf{B}, \quad (6)$$

$$\vec{\omega} = \nabla \times \mathbf{v}, \quad (7)$$

where μ_0 is the vacuum magnetic permeability, γ is the adiabatic constant, ν and ν_n are artificial viscosity and diffusion coefficients chosen to maintain numerical stability and all the other quantities are conventional. The subscript 'eq' represents the equilibrium variables. The energetic-ion contribution is included in the MHD momentum equation (equation (2)) as the energetic-ion current density. The quantity \mathbf{j}'_h is the energetic-ion current density without $\mathbf{E} \times \mathbf{B}$ drift. We see that electromagnetic field is given by the standard MHD description. This model is accurate under the condition that

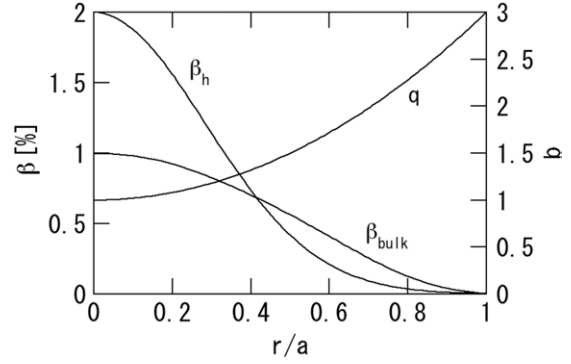


Figure 1. Spatial profiles of energetic-ion beta, bulk plasma beta and safety factor.

the energetic-ion density is much less than the bulk plasma density.

The MHD equations are solved using a fourth order (in both space and time) finite difference scheme. The drift-kinetic description [19] is employed for the energetic ions. The energetic-ion current density \mathbf{j}'_h in equation (2) includes the contributions from parallel velocity, magnetic curvature and gradient drifts and magnetization current. The $\mathbf{E} \times \mathbf{B}$ drift disappears in \mathbf{j}'_h due to the quasi-neutrality [13]. The computational particles are initially loaded uniformly in the phase space.

For the purpose of clarifying the nonlinear MHD effects, the linear-MHD calculations were performed to solve the following equations:

$$\frac{\partial \rho}{\partial t} = -\nabla \cdot (\rho_{eq} \mathbf{v}) + \nu_n \Delta (\rho - \rho_{eq}), \quad (8)$$

$$\begin{aligned} \rho_{eq} \frac{\partial \mathbf{v}}{\partial t} = & -\nabla p + (\mathbf{j}_{eq} - \mathbf{j}'_{heq}) \delta \mathbf{B} \\ & + (\delta \mathbf{j} - \delta \mathbf{j}'_h) \times \mathbf{B}_{eq} + \frac{4}{3} \nabla (\nu \rho_{eq} \nabla \cdot \mathbf{v}) \\ & - \nabla \times (\nu \rho_{eq} \vec{\omega}), \end{aligned} \quad (9)$$

$$\frac{\partial \mathbf{B}}{\partial t} = -\nabla \times \mathbf{E}, \quad (10)$$

$$\begin{aligned} \frac{\partial p}{\partial t} = & -\nabla \cdot (p_{eq} \mathbf{v}) - (\gamma - 1) p_{eq} \nabla \cdot \mathbf{v} \\ & + (\gamma - 1) \eta \delta \mathbf{j} \cdot \mathbf{j}_{eq} + \nu_n \Delta (p - p_{eq}), \end{aligned} \quad (11)$$

$$\mathbf{E} = -\mathbf{v} \times \mathbf{B}_{eq} + \eta \delta \mathbf{j}. \quad (12)$$

Here the variables with δ such as $\delta \mathbf{B}$ represent the fluctuations, for example, $\delta \mathbf{B} = \mathbf{B} - \mathbf{B}_{eq}$.

A tokamak plasma with the aspect ratio of $R_0/a = 3.2$ was investigated where R_0 and a represent the major radius of the geometrical centre of the simulation domain and the plasma minor radius, respectively. The cylindrical coordinates (R, φ, z) are employed. The shape of the outermost magnetic surface is circular. The spatial profiles of the energetic-ion beta, bulk plasma beta and safety factor are shown in figure 1. The bulk plasma density is uniform. The different initial values of the central energetic-ion beta β_{h0} were investigated with the profile kept constant. The central energetic-ion beta β_{h0} shown in figure 1 is 2.0%. The initial velocity-space distribution

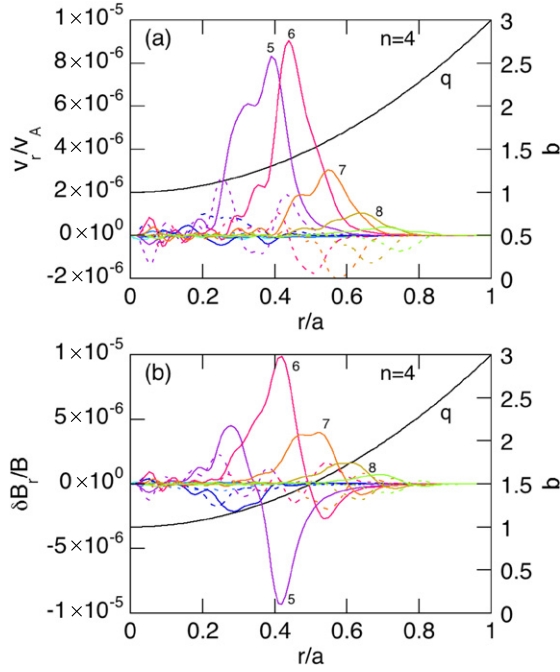


Figure 2. Spatial profiles of each poloidal harmonic of the TAE with toroidal mode number $n = 4$ for (a) radial velocity and (b) radial magnetic field. Solid (dashed) lines show $\cos(m\vartheta + n\phi)$ [$\sin(m\vartheta + n\phi)$] harmonics with poloidal mode number m labelled in the figure.

of the energetic ions is a slowing-down distribution with a maximum velocity $1.2v_A$ and the critical velocity $0.5v_A$, where v_A denotes the Alfvén velocity at the plasma centre. The ratio of the energetic-ion Larmor radius to the minor radius is $1/16$ for the energetic-ion velocity equal to the Alfvén velocity. The number of grid points for the cylindrical coordinates (R, φ, z) is $128 \times 64 \times 128$ and the number of computational particles is 5.2×10^5 . We investigate the evolution of the $n = 4$ mode, which is an exact solution of the equations of a quarter of the tokamak domain with the toroidal angle taken from $0 \leq \varphi \leq \pi/2$. The MHD nonlinearities generate fluctuations with toroidal mode numbers that are multiples of 4 ($n = 0, 4, 8, 12, 16, \dots$). In contrast, in the linear-MHD code only the $n = 4$ component is excited. The nonlinear evolution of the energetic ions generates the current density fluctuation $\delta j'_h$ with a harmonic content in φ , with all harmonics being a multiple of 4. This leads to the generation of MHD fluctuations with toroidal mode numbers that are multiples of $n = 4$ and obscures the effects of the MHD nonlinearity. Then, we retain only the $n = 4$ harmonic of the hot particle current, while we artificially remove the energetic-ion current density fluctuation $\delta j'_h$ if $n \neq 4$. The viscosity, diffusion and resistivity coefficients in the MHD equations are chosen to be $\nu = \nu_n = 10^{-6}v_A R_0$ and $\eta = 10^{-6}\mu_0 v_A R_0$, respectively. The spatial profile of the unstable $n = 4$ TAE mode observed at the linearly growing phase of the instability for $\beta_{h0} = 1.0\%$ is shown in figure 2. The phase of the mode in the figure is chosen so that the cosine part of the dominant harmonic $m/n = 6/4$ is maximized at the peak location. The frequency and growth rate of the TAE are $\omega = 0.318\omega_A$, $\gamma = 1.3 \times 10^{-2}\omega_A$ with $\omega_A = v_A/R_{axis}$, where R_{axis} is the major radius of the magnetic axis. The maximum values of v_r/v_A and $\delta B_r/B$ are close to each other for the TAE,

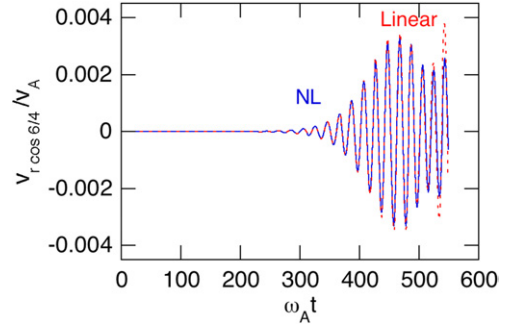


Figure 3. Comparison of radial velocity evolution for the linear-MHD and the nonlinear MHD runs using the cosine part of $m/n = 6/4$ harmonics at $r/a = 0.42$ for $\beta_{h0} = 1.5\%$.

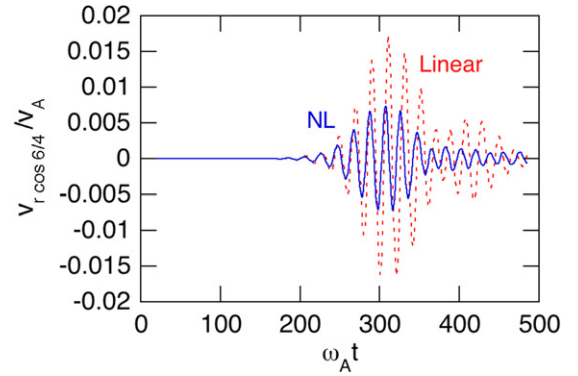


Figure 4. Comparison of radial velocity evolution for the linear-MHD and the nonlinear MHD runs using the cosine part of $m/n = 6/4$ harmonics at $r/a = 0.42$ for $\beta_{h0} = 2.0\%$.

because a relation between velocity and magnetic fluctuations $|v_r/v_A| = |\delta B_r/B|$ holds for shear Alfvén waves in a uniform plasma. The major harmonics ($m/n = 5/4$ and $6/4$) of the radial magnetic field profiles have opposite signs whereas the signs of the radial velocity harmonics are the same. The parallel wave number $k_{\parallel} = (n - m/q)/R_0$ is positive for $m/n = 5/4$ and negative for $m/n = 6/4$ in the region $5/4 < q < 6/4$ ($0.35 < r/a < 0.50$). The opposite sign of the parallel wave number leads to the opposite sign of the magnetic field fluctuation. For the purpose of the data analysis, magnetic flux coordinates (r, φ, ϑ) , where r is the radial coordinate and ϑ is the poloidal angle, were constructed for the MHD equilibrium.

3. Simulation results

3.1. Comparison of linear-MHD and nonlinear MHD simulations

The evolution of the MHD radial velocity is compared in figures 3 and 4 for the linear-MHD simulation and the nonlinear MHD simulation. A comparison of the radial velocity excitation is made for two different hot particle beta values, $\beta_{h0} = 1.5\%$ and $\beta_{h0} = 2.0\%$. Figures 3 and 4 show the evolution of the $m/n = 6/4$ harmonics of radial velocity v_r/v_A measured at the TAE peak location $r = 0.42a$. The frequency and growth rate are $\omega = 0.310\omega_A$, $\gamma = 3.0 \times 10^{-2}\omega_A$ for $\beta_{h0} = 1.5\%$, and $\omega = 0.303\omega_A$, $\gamma = 5.1 \times 10^{-2}\omega_A$ for $\beta_{h0} = 2.0\%$. We see in figure 3 that the saturation levels

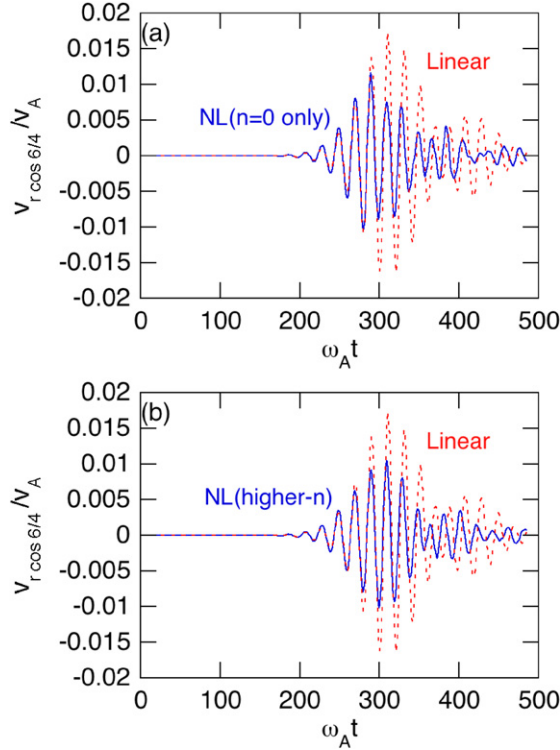


Figure 5. Comparison of radial velocity evolution for cosine part of $m/n = 6/4$ harmonics at $r/a = 0.42$ for $\beta_{h0} = 2.0\%$ between the linear-MHD and the nonlinear MHD runs (a) with only $n = 0$ and 4 modes retained and (b) without $n = 0$, but with $n = 4, 8$, and higher- n modes retained.

of v_r/v_A for both the linear-MHD and nonlinear MHD runs are $\sim 3 \times 10^{-3}$ and in the two calculations the phases of the excitation remain synchronized in time, indicating in this case a robust accuracy of the reduced model. On the other hand, for $\beta_{h0} = 2.0\%$, a significant reduction in the saturation level can be seen for the nonlinear MHD run in figure 4. The saturation level of v_r/v_A is $\sim 8 \times 10^{-3}$ for the nonlinear MHD simulation while it is $\sim 1.7 \times 10^{-2}$ for the linear-MHD simulation. The MHD nonlinear effects reduce the TAE saturation level by half when it reaches $v_r/v_A \sim \delta B_r/B \sim 10^{-2}$. For cases where the instability growth is lower, the saturation level is $v_r/v_A \sim \delta B_r/B \sim 10^{-3}$ and the MHD nonlinearity does not play any important role. Then the saturation mechanism is dominated by the particle nonlinear dynamics, i.e. the particle trapping by the TAE causes the saturation.

In the evolution of the TAE mode, the nonlinear terms in the MHD equations generate the fluctuations with toroidal mode numbers multiples of 4 ($n = 0, 4, 8, 12, 16, \dots$). It is interesting to investigate which toroidal mode number is important for the TAE saturation level reduction. We conducted two types of nonlinear MHD simulations. In the first type, only the $n = 0$ and 4 modes are retained while the higher- n ($n \geq 8$) modes are artificially removed. In the second type, only the $n = 4$ and higher- n modes are retained without $n = 0$ fluctuations. The results are compared in figure 5 with that of the linear-MHD simulation. We can see that both the $n = 0$ and higher- n modes reduce the TAE saturation level.

3.2. Physics mechanism of saturation level reduction

In this subsection, we discuss the physics mechanism that reduces the TAE saturation level. We focus on the energy dissipation that appears in equation (4) from the viscous heating and the Joule heating terms. They are, respectively, in proportion to viscosity ν and resistivity η . We analysed the time evolution of the energy and energy dissipation for each toroidal mode number n for the initial central energetic-ion beta $\beta_{h0} = 1.7\%$. For this case, the TAE saturation level in the nonlinear MHD simulation is reduced by nearly half to $v_r/v_A \sim 6 \times 10^{-3}$, while it is $v_r/v_A \sim 1.0 \times 10^{-2}$ for the linear-MHD simulation.

The MHD fluctuation energy is given by

$$E = \int \left(\frac{1}{2} \rho v^2 + \frac{B^2 - B_{eq}^2}{2\mu_0} + \frac{\delta p}{\gamma - 1} \right) dV. \quad (13)$$

We decompose the MHD fluctuations for each toroidal mode number $n \geq 0$. For example, the velocity fluctuation is decomposed into

$$v_n(R, \varphi, z) = v_{nc}(R, z) \cos(n\varphi) + v_{ns}(R, z) \sin(n\varphi), \quad (14)$$

$$\begin{aligned} v_{nc}(R, z) &= \frac{4}{\pi} \int_0^{\pi/2} v(R, \varphi, z) \cos(n\varphi) d\varphi \\ v_{ns}(R, z) &= \frac{4}{\pi} \int_0^{\pi/2} v(R, \varphi, z) \sin(n\varphi) d\varphi \quad (\text{for } n \neq 0) \end{aligned} \quad (15)$$

$$v_{nc}(R, z) = \frac{2}{\pi} \int_0^{\pi/2} v(R, \varphi, z) d\varphi, \quad v_{ns}(R, z) = 0 \quad (\text{for } n = 0). \quad (16)$$

The MHD kinetic energy is expressed in terms of the harmonics of density and velocity

$$\int \frac{1}{2} \rho v^2 dV = \sum_{l+m=k \text{ or } |l-m|=k} \int \frac{1}{2} \rho_k v_l \cdot v_m dV \quad (k, l, m \geq 0). \quad (17)$$

We neglect the terms with $k \neq 0$ because $\rho_0 = \rho_{eq} + \delta\rho_0 \gg \delta\rho_{k \neq 0}$ holds. Then, the MHD fluctuation energy is written as the sum of energy over the toroidal mode numbers

$$E = \sum_n E_n, \quad (18)$$

$$E_n \equiv \int \left(\frac{1}{2} \rho_0 v_n^2 + \frac{2\delta B_n \cdot B_{eq} + \delta B_n^2}{2\mu_0} + \frac{\delta p_n}{\gamma - 1} \right) dV. \quad (19)$$

For $n \neq 0$, E_n is reduced to

$$E_n \equiv \int \left(\frac{1}{2} \rho_0 v_n^2 + \frac{1}{2\mu_0} \delta B_n^2 \right) dV, \quad (20)$$

because the terms $\delta B_n \cdot B_{eq}$ and δp_n vanish after integration over the toroidal angle.

We also analyse the evolution of the energy dissipation for each toroidal mode number n

$$D_n = \int \left[\nu \rho_0 \omega_n^2 + \frac{4}{3} \nu \rho_0 (\nabla \cdot \mathbf{v}_n)^2 + \eta \delta \mathbf{j}_n \cdot \mathbf{j}_n \right] dV. \quad (21)$$

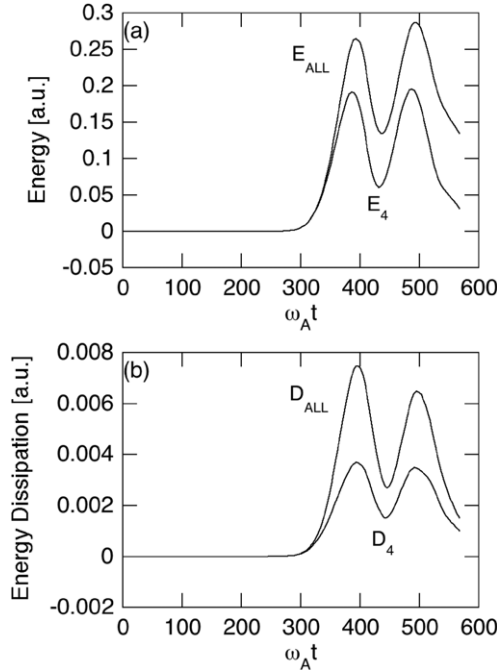


Figure 6. Evolution of (a) energy and (b) energy dissipation with toroidal mode number $n = 4$ denoted as E_4 and D_4 along with the total energy and total energy dissipation of toroidal mode numbers $n = 0, 4, 8, 12, 16$ denoted as E_{ALL} and D_{ALL} for $\beta_{h0} = 1.7\%$.

For $n = 0$, we investigate an alternative form of the fluctuation energy, S and E'_0 , defined by

$$\begin{aligned} \frac{d}{dt} S &\equiv D_{\text{ALL}} \equiv \sum_n D_n, & S_{t=0} &= 0 \\ E'_0 &\equiv E_0 - S. \end{aligned} \quad (22)$$

For the purpose of the saturation analysis, E_0 is not a useful variable because E_0 monotonically increases in time, as all the dissipated energy is transferred to the $n = 0$ mode. We have found that E'_0 is a useful variable to understand the saturation process of the instability, as is discussed below.

The evolution of energy with toroidal mode number $n = 4$ (E_4) and the sum of energy over toroidal mode numbers $n = 0, 4, 8, 12, 16$ ($E_{\text{ALL}} = E'_0 + E_4 + E_8 + E_{12} + E_{16}$) is shown in figure 6(a). At saturation time, $\omega_A t = 380$, of the TAE instability, the energy in the toroidal mode numbers $n = 12$ (E_{12}) and 16 (E_{16}) are, respectively, 3% and 1% of the energy of the $n = 4$ (E_4) component. The energy of the modes with $n \geq 20$ is negligibly small and the energy and dissipation were not analysed, although such higher- n modes are included in the simulation. We also see in figure 6(a) that at saturation the total energy E_{ALL} is greater than the energy of the $n = 4$ mode E_4 by 40%. The total energy dissipation of toroidal mode numbers $n = 0, 4, 8, 12, 16$ ($D_{\text{ALL}} = D_0 + D_4 + D_8 + D_{12} + D_{16}$) is compared with that of $n = 4$ (D_4) in figure 6(b). The total dissipation is two times greater than the dissipation in $n = 4$ alone.

Let us consider why the saturation level is reduced by the MHD nonlinearity. The energy evolution for each toroidal

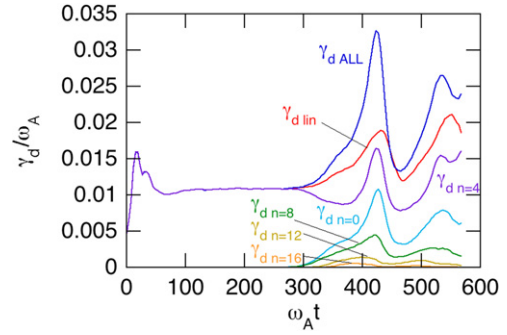


Figure 7. Evolution of damping rate for each toroidal mode number and total damping rate in the nonlinear MHD simulation, and damping rate in the linear-MHD simulation ($\gamma_{d \text{ lin}}$) for $\beta_{h0} = 1.7\%$.

mode number is given by

$$\begin{aligned} \frac{d}{dt} E_4 &= 2\gamma_h(t) E_4 - D_4 + P_4, \\ \frac{d}{dt} E'_0 &= -D_0 + P_0, \\ \frac{d}{dt} E_n &= -D_n + P_n \quad (n \neq 0, 4), \end{aligned} \quad (23)$$

where $\gamma_h(t)$ represents the energetic-particle drive and P_n is the energy transfer from the other toroidal mode numbers. The factor of 2 arises for $\gamma_h(t)$, which denotes the amplitude growth rate. The energetic-particle drive is restricted only to the $n = 4$ mode in this work. When the nonlinear coupling is so weak that P_n can be neglected, the saturation condition for the $n = 4$ mode is given by $\gamma_h(t) = D_4/2E_4$. As the TAE amplitude grows, the particle trapping reduces $\gamma_h(t)$ to $\gamma_{d4} = D_4/2E_4$ that is the damping rate of the $n = 4$ mode, leading to the saturation of the instability. For the case investigated here, the nonlinear coupling cannot be neglected. The summation of all equations (23) gives

$$\frac{d}{dt} E_{\text{ALL}} = \frac{d}{dt} \left(E'_0 + \sum_{n \neq 0} E_n \right) = 2\gamma_h(t) E_4 - D_{\text{ALL}}. \quad (24)$$

Here, we used the relation $\sum_n P_n = 0$ for energy conservation. As we see in figure 6(a), the saturation of E_4 and E_{ALL} takes place roughly at the same time. Then, we investigate the saturation condition of E_{ALL} instead of E_4 . The saturation condition of E_{ALL} is given by $\gamma_h(t) = D_{\text{ALL}}/2E_4$, which is a higher level of the energetic-particle drive than that for the linear-MHD run, corresponding to the earlier saturation of the instability. We can say that $D_{\text{ALL}}/2E_4$ is an effective damping rate for the cases where nonlinear coupling between the different toroidal mode numbers is essential. In figure 7 the evolution of $\gamma_{d n} = D_n/2E_n$ and $\gamma_{d \text{ ALL}} = D_{\text{ALL}}/2E_4$ are compared with $\gamma_{d \text{ lin}} = D_4/2E_4$ in the relevant linear-MHD simulation. The total damping rate $\gamma_{d \text{ ALL}}$, in the nonlinear MHD simulation, is clearly greater than the $n = 4$ TAE damping rate $\gamma_{d \text{ lin}}$ in the linear-MHD simulation. This explains why the saturation level is reduced by the MHD nonlinearity. The nonlinear coupling increases the total energy dissipation leading to the lower saturation level.

3.3. Effects of weak dissipation

As we mentioned in section 2, the viscosity, diffusion and resistivity coefficients employed in the previous subsections and in the next subsection are chosen to be $\nu = \nu_n = 10^{-6} v_A R_0$ and $\eta = 10^{-6} \mu_0 v_A R_0$. Of course, in realistic fusion experiment plasmas the dissipation coefficients are lower by orders of magnitude. For example, normalized resistivity is $\eta \sim 10^{-9} \mu_0 v_A R_0$ for hydrogen plasma with electron temperature 1 keV, ion density 10^{19} m^{-3} , magnetic field 1 T and major radius 3 m. Thus, it is important to examine the effects of weak dissipation. On the other hand, simulation with lower dissipation coefficients needs a larger number of grid points. As the dissipation terms are second-order spatial derivatives, dissipation coefficients that are three orders of magnitude lower need $10^{1.5}$ times larger number of numerical grid points in one direction. This leads to $10^{4.5}$ times larger number of total grid points. Since such a simulation is not possible at the present time, we investigate the effects of weak dissipation by simulating a case with diffusion coefficients reduced by 1/4 to $\nu = \nu_n = 2.5 \times 10^{-7} v_A R_0$ and $\eta = 2.5 \times 10^{-7} \mu_0 v_A R_0$. The number of grid points for each of the cylindrical coordinates is doubled leading to $256 \times 128 \times 256$ grid points for (R, φ, z) . The number of computational particles is increased by a factor of 8 to 4.2×10^6 . The radial velocity evolution is compared in figure 8(a) for the linear-MHD and the nonlinear MHD runs for $\beta_{h0} = 1.7\%$. The saturation level of v_r/v_A is $\sim 7 \times 10^{-3}$ for the nonlinear MHD simulation while it is $\sim 1.4 \times 10^{-2}$ for the linear-MHD simulation. We thereby demonstrate again the reduction in the saturation amplitude by the nonlinear MHD effects but now with weaker dissipation. For the linear-MHD run, another unstable TAE with major harmonics $m/n = 6/4$ and $7/4$ affects the evolution of the TAE focused on in this paper, leading to the second amplitude peak higher than the first peak.

Shown in figure 8(b) is both the evolution of the damping rate for each toroidal mode number together with the total damping rate in the nonlinear MHD simulation and the damping rate in the linear-MHD simulation. Comparing the results for the lower with the higher dissipation case shown in figure 7, we find that in the lower dissipation case we have a lower damping rate for the linearly growing phase prior to $\omega_A t = 250$. However, the total damping rate $\gamma_d \text{ ALL}$ increases in the nonlinear phase, just in the same way as the stronger dissipation case illustrated in figure 7. As seen from figure 8(b), the damping rate for the higher- n modes increases significantly in the nonlinear phase leading to the high level of the total damping rate. This result suggests that the saturation level would similarly reduce by the nonlinear MHD effects even if the parameters for more realistic dissipation were taken into account. We would also like to point out that a mechanism for substantial dissipation of higher- n modes might be arising from the continuum damping that does not depend on the dissipation coefficients [20, 21] yet exists within an MHD model. Further work to verify this conjecture is needed.

3.4. Spatial profile and evolution of nonlinearly generated modes

Let us examine the spatial profiles and the evolution of the nonlinearly generated modes. We have analysed the spatial

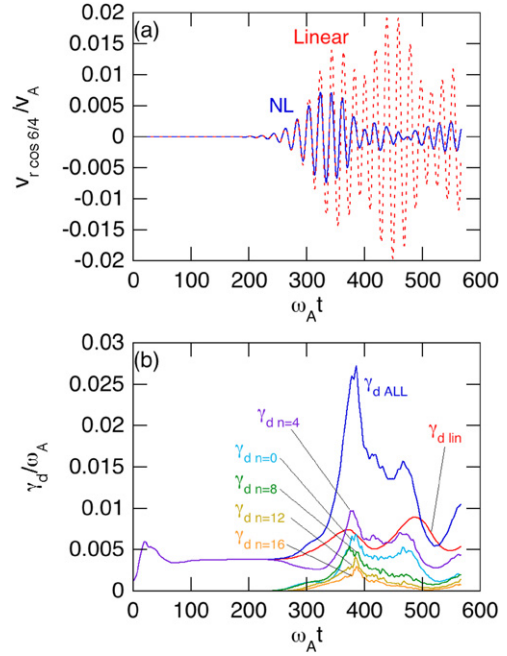


Figure 8. Comparison of the radial velocity evolution for the linear-MHD and the nonlinear MHD runs using the cosine part of $m/n = 6/4$ harmonics at $r/a = 0.42$ (a), and evolution of damping rate for each toroidal mode number and total damping rate in the nonlinear MHD simulation, and damping rate in the linear-MHD simulation ($\gamma_d \text{ lin}$) (b) for $\beta_{h0} = 1.7\%$ and $\nu = \eta/\mu_0 = \nu_n = 2.5 \times 10^{-7} v_A R_0$.

profiles of the $n = 0$ poloidal flow for different times of the nonlinear MHD simulation with $\beta_{h0} = 2.0\%$. The radial velocity evolution for the $n = 4$ mode was already shown in figure 4. The spatial profiles of the $n = 0$ poloidal flow at $\omega_A t = 189$ and $\omega_A t = 227$ are shown in figure 9. When we compare figures 9(a) and (b), we see that the $n = 0$ poloidal flow profile remains constant during the linear phase of the TAE instability. The profile peaks at the maximum position of the TAE mode amplitude. The largest harmonics are the $m/n = 0/0$ and $1/0$ cosine ($\propto \cos \vartheta$) harmonics. The evolution of the $0/0$ harmonic of the poloidal flow, namely the zonal flow, is shown in figure 10(a) along with the $1/0$ sine harmonic of the pressure fluctuation. The amplitude evolution of the zonal flow and the principal harmonic of the TAE radial velocity at the same magnetic surface are shown in figure 10(b). As can be seen in figure 10(a), the zonal flow and the pressure oscillate with the same frequency after the saturation of the instability. This oscillation is a GAM because the frequency of the oscillation $\omega = 0.11\omega_A$ is close to the theoretical GAM frequency $\omega_{\text{GAM}} = \omega_A \sqrt{\gamma \beta_{\text{bulk}} (1 + 1/2q^2)} = 0.12\omega_A$ [22, 23]. Furthermore, the coupling between the zonal flow and the $1/0$ sine harmonic of the pressure fluctuation is consistent with the theory of GAM. We see in figure 10(b) that the zonal flow amplitude grows at twice the TAE growth rate. This suggests that the $n = 0$ modes are primarily generated by the coupling of two $n = 4$ harmonics of the TAE mode.

Let us discuss the $n = 0$ mode in its exponentially growing phase and how the GAM is excited. When the $n = 0$ mode amplitude is sufficiently small and the source generated by the nonlinear coupling is neglected, the $n = 0$ mode evolution can be described by the linear MHD equations (8)–(11). This can

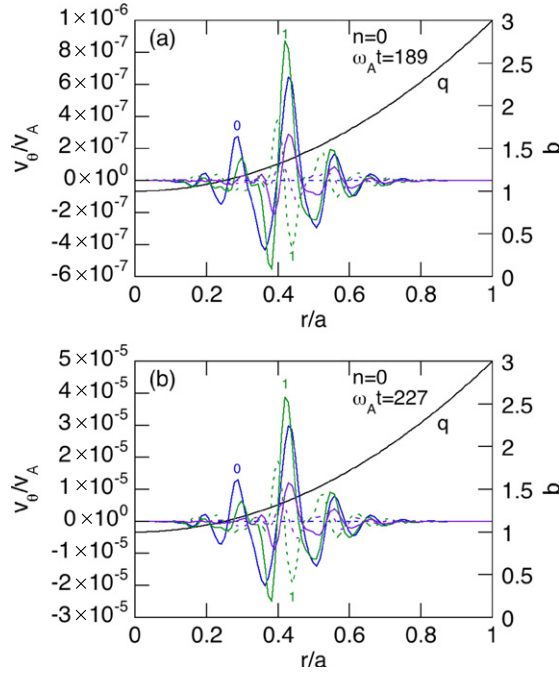


Figure 9. Spatial profile of each poloidal harmonic of the poloidal flow with $n = 0$ during the linearly growing phase of the TAE instability at (a) $\omega_A t = 189$ and (b) $\omega_A t = 227$ for $\beta_{h0} = 2.0\%$. Solid (dashed) lines show $\cos(m\vartheta)$ [$\sin(m\vartheta)$] harmonics with poloidal mode number m labelled in the figure.

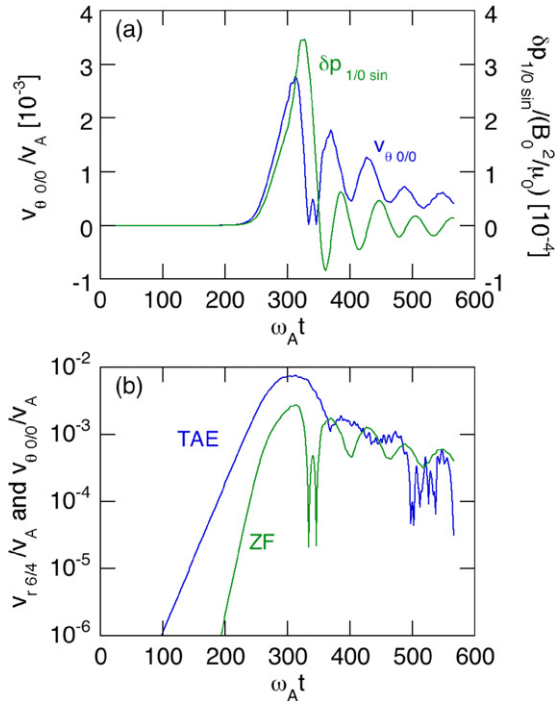


Figure 10. Time evolution of (a) the zonal flow and pressure fluctuation and (b) the zonal flow amplitude and the TAE amplitude for $\beta_{h0} = 2.0\%$.

be expressed in the following form

$$\frac{\partial}{\partial t} z + M_{\text{eq}}(z) = 0, \quad (25)$$

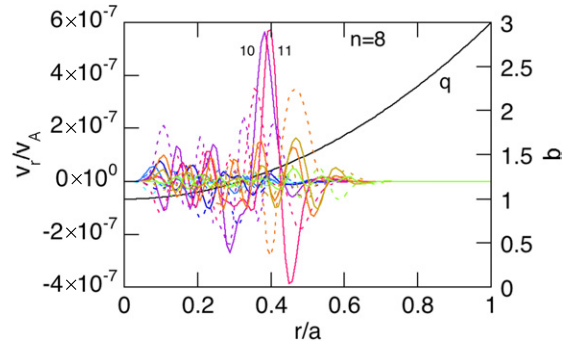


Figure 11. Spatial profile of each poloidal harmonic of the radial velocity with $n = 8$ during the linearly growing phase of the TAE instability. Solid (dashed) lines show $\cos(m\vartheta + n\varphi)$ [$\sin(m\vartheta + n\varphi)$] harmonics with poloidal mode number m labelled in the figure.

where z is the $n = 0$ mode fluctuations $z = {}^t(\delta\rho, \delta v, \delta B, \delta p)$ and M_{eq} is the linear-MHD operator which is a function of the equilibrium variables. Next we consider the source vector s which is generated by the nonlinear coupling of the TAE eigenfunction. The evolution of z at the linear phase is described by

$$\frac{\partial}{\partial t} z + M_{\text{eq}}(z) = s. \quad (26)$$

The source vector can be expressed as $s = s_0 e^{2\gamma_{\text{TAE}} t}$ using the TAE growth rate γ_{TAE} because the nonlinear coupling of the TAE eigenvectors generates the $n = 0$ fluctuations with zero frequency and growth rate $2\gamma_{\text{TAE}}$. We also see from the simulation results shown in figures 9 and 10 that the $n = 0$ mode fluctuations can be expressed as $z = z_0 e^{2\gamma_{\text{TAE}} t}$. Here, s_0 and z_0 are independent of time. Equation (26) is reduced to

$$2\gamma_{\text{TAE}} I(z_0) + M_{\text{eq}}(z_0) = [2\gamma_{\text{TAE}} I + M_{\text{eq}}](z_0) = s_0, \quad (27)$$

where I is the unit operator and both I and M_{eq} are linear operators of z_0 . Then, the spatial profile of the $n = 0$ mode fluctuations is given by $z_0 = (2\gamma_{\text{TAE}} I + M_{\text{eq}})^{-1}(s_0)$. The zonal flow profile shown in figure 9 is a part of the solution z_0 that contains the $n = 0$ fluctuations of all the MHD variables. It should be emphasized that the spatial profile z_0 depends on $2\gamma_{\text{TAE}}$, the growth rate of the nonlinear source during the TAE linear phase. When the instability saturates, the growth rate of the nonlinear source approaches zero. Then, the $n = 0$ field z_0 that is matched to the TAE linear growth is no longer a solution of equation (26) during the nonlinear phase. This leads to the excitation of the $n = 0$ MHD waves that include the GAM.

The spatial profiles of the $n = 8$ harmonics have also been investigated. The radial velocity profile is shown in figure 11. The profile peaks at the TAE peak location. The largest harmonics are $m/n = 10/8$ and $11/8$. The $m/n = 11/8$ harmonic is consistent with the nonlinear source generated by the coupling of the TAE harmonics $m/n = 5/4$ and $6/4$. The $m/n = 10/8$ harmonic may be generated from the nonlinear source with $m/n = 11/8$ through toroidal coupling. The evolution of the $11/8$ harmonic and the frequency is shown in figure 12. We see in figure 12(b) that the real frequency of the $n = 8$ mode is twice the TAE frequency.

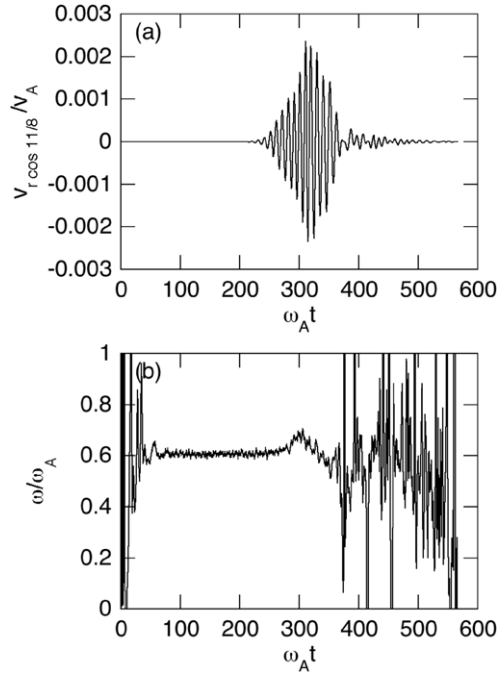


Figure 12. Time evolution of (a) the cosine part of $m/n = 11/8$ radial velocity harmonics and (b) the frequency for $\beta_{h0} = 2.0\%$.

4. Discussion and summary

The nonlinear MHD effects on the evolution of the Alfvén eigenmode were investigated with hybrid simulations of an MHD fluid interacting with energetic particles. To clarify the role of the MHD nonlinearity, the nonlinear MHD results were compared with results from a reduced model, where only linear-MHD equations were solved together with a nonlinear response of the energetic particles. Specifically, we studied the evolution of an $n = 4$ TAE mode destabilized by its resonant interaction with energetic particles in a tokamak plasma. When the TAE saturation level is $\delta B/B \leq 10^{-3}$ no significant difference was found between the results of the linear-MHD simulation and the nonlinear MHD simulations. On the other hand, when in the linear-MHD simulation the TAE saturation level is $\delta B/B \sim 10^{-2}$, the saturation level in the nonlinear MHD case is found to be reduced to half the result of the linear-MHD simulation. We found that the nonlinearly generated $n = 0$ and the higher- n ($n \geq 8$) modes provide increased energy dissipation that appears crucial for achieving a reduced TAE saturation level.

The effects of MHD nonlinearities on the increase in TAE damping rate were discussed in previous works [11, 12]. We found in this work that the total damping rate of all the toroidal mode numbers increases before the saturation of the instability. The increased dissipation leads to the reduction in the saturation amplitude even though the damping rate of the $n = 4$ component, which was the original TAE carrier, decreases slightly before saturation. We emphasize that this is a new picture for the mechanism by which nonlinear MHD effects cause saturation that is different from the previous works. In the simulation results of the TAE bursts presented in [1], the energetic-particle loss takes place when the TAE amplitude reaches $\delta B/B \sim 5 \times 10^{-3}$ while

the saturation amplitude is $\delta B/B \sim 2 \times 10^{-2}$. It was also demonstrated in another study [10] that synchronized bursts of multiple TAEs take place when the MHD nonlinearities are taken into account. In contrast, in this work, we have focused on the evolution of a single TAE and demonstrated that the nonlinear MHD effects reduce the TAE saturation level. Computer simulations of multiple Alfvén eigenmodes have been conducted [6, 10, 12, 24]. There is still a need to investigate the nonlinear MHD effects in multiple mode evolution by comparing the linear and nonlinear MHD simulations as has been performed in this work. For future work, it is important to reproduce the TAE bursts, using realistic parameters. The challenge is to demonstrate saturation amplitudes that are closer to the value inferred from the experimental plasma displacement measurements.

Another interesting discovery of this work is the excitation of the GAM after the saturation of the TAE instability. In the linearly growing phase of the instability, the zonal fluctuations are matched to the growth of the nonlinear source, with a spatial profile kept constant. When the instability saturates, however, the spatial profile of the zonal fluctuations is no longer matched to the evolution of the nonlinear source. This excites the $n = 0$ MHD waves that includes the GAM. It is evident that the GAM is excited through the nonlinear MHD effect because the $n = 4$ fluctuations of the energetic-particle current density retained in the simulations cannot directly drive the GAM. This excitation mechanism of the GAM is different from the direct destabilization by the energetic particles [25, 26]. We note that the excitation of zonal flow and GAM through the TAE nonlinearity is an interesting phenomenon for burning plasmas since its excitation may lead to improved plasma confinement and to bulk plasma heating through the damping of the GAM.

Acknowledgments

Numerical computations were performed at the Plasma Simulator (HITACHI SR16000) of the National Institute for Fusion Science. This work was supported by a Grant-in-Aid for Scientific Research from the Japan Society for the Promotion of Science (No 20340165).

References

- [1] Todo Y., Berk H.L. and Breizman B.N. 2003 *Phys. Plasmas* **10** 2888
- [2] Wong K.L. *et al* 1991 *Phys. Rev. Lett.* **66** 1874
- [3] Durst R.D., Fonck R.J., Wong K.L., Cheng C.Z., Fredrickson E.D. and Paul S.F. 1992 *Phys. Fluids B* **4** 3707
- [4] Berk H.L. and Breizman B.B. 1990 *Phys. Fluids B* **2** 2246
- [5] Berk H.L., Breizman B.N. and Ye H. 1993 *Phys. Fluids B* **5** 1506
- [6] Fu G.Y. and Park W. 1995 *Phys. Rev. Lett.* **74** 1594
- [7] Todo Y., Sato T., Watanabe K., Watanabe T.H. and Horiuchi R. 1995 *Phys. Plasmas* **2** 2711
- [8] Wu Y., White R.B., Chen Y. and Rosenbluth M.N. 1995 *Phys. Plasmas* **2** 4555
- [9] Briguglio S., Zonca F. and Vlad G. 1998 *Phys. Plasmas* **5** 3287
- [10] Todo Y., Watanabe T.-H., Hyoung-Bin Park and Sato T. 2001 *Nucl. Fusion* **41** 1153
- [11] Zonca F., Romanelli F., Vlad G. and Kar C. 1995 *Phys. Rev. Lett.* **74** 698
- [12] Spong D.A., Carreras B.A. and Hedrick C.L. 1994 *Phys. Plasmas* **1** 1503

- [13] Todo Y. and Sato T. 1998 *Phys. Plasmas* **5** 1321
- [14] Todo Y., Shinohara K., Takechi M. and Ishikawa M. 2005 *Phys. Plasmas* **12** 012503
- [15] Todo Y. 2006 *Phys. Plasmas* **13** 082503
- [16] Park W. *et al* 1992 *Phys. Fluids B* **4** 2033
- [17] Spong D.A., Carreras B.A. and Hedrick C.L. 1992 *Phys. Fluids B* **4** 3316
- [18] Briguglio S., Vlad G., Zonca F. and Kar C. 1995 *Phys. Plasmas* **2** 3711
- [19] Littlejohn R.G. 1981 *Phys. Fluids* **24** 1730
- [20] Zonca F. and Chen L. 1992 *Phys. Rev. Lett.* **68** 592
- [21] Rosenbluth M.N., Berk H.L., Van Dam J.W. and Lindberg D.M. 1992 *Phys. Rev. Lett.* **68** 596
- [22] Winsor N., Johnson J.L. and Dawson J.M. 1968 *Phys. Fluids* **11** 2448
- [23] Hassam A.B. and Drake J.F. 1993 *Phys. Fluids B* **5** 4022
- [24] Vlad G. *et al* 2009 *Nucl. Fusion* **49** 075024
- [25] Berk H.L. *et al* 2006 *Nucl. Fusion* **46** S888
- [26] Fu G.Y. 2008 *Phys. Rev. Lett.* **101** 185002